Very-high-cycle fatigue induced growth and amorphization of Si particles in additively manufactured AlSi10Mg alloy: Dependence of applied stress ratio

Jianghua Li [a], Jingyu Sun [a], Yajing Li [b], Guian Qian [a,*], Zhiyang Wang [c,*]

[a] State Key Laboratory of Nonlinear Mechanics (LNM), Institute of Mechanics, Chinese Academy of Sciences, Beijing 100190, China
[b] School of Chemical Engineering and Technology, Tianjin University, Tianjin, China
[c] Australian Nuclear Science and Technology Organisation (ANSTO), Sydney, NSW 2234, Australia

ARTICLE INFO

ABSTRACT

The microstructural evolution at the fracture surface in response to very-high-cycle fatigue (VHCF) under stress ratios (R) of −1 and 0.5 in an AlSi10Mg alloy produced by Laser Powder Bed Fusion was investigated. The results show that appreciable growth of the Si precipitates at the cellular network boundaries in the as-built microstructure was observed under R = −1. Moreover, significant amorphization of the initial crystalline Si precipitates occurred in the vicinity of the fracture surface under this condition. A layer of fine Al grains was developed in the "fish-eye" region of the fracture surface. These microstructural responses are rationalized by the generation of lattice defects including dislocations and sub-grain boundaries during cyclic pressing of crack surfaces under R = −1, which mediates the Si solute diffusion and re-precipitation in the alloy as well as the amorphization of initial Si crystalline precipitation. In contrast, far fewer dislocations were observed near the crack surfaces under R = 0.5, which is attributed to the absence of cyclic pressing of crack surfaces and severe plastic deformation in this scenario. This work provides insights into the stress ratio dependence of the microstructural evolution in the fatigued Al alloys. The obtained knowledge is useful for future understanding of the fatigue failure in Al alloys produced by additive manufacturing.

1. Introduction

Al-Si alloys possess a combination of high specific strength, good corrosion resistance and castability, showing competitive advantages over a wide range of applications in automotive and aerospace industries [1]. Under the operational conditions of transportation, the Al-alloy components often experience an alternating stress lower than their monotonic yield strength with significant loading cycles accumulated beyond 10^7 over their life-time, i.e., the very-high-cycle fatigue (VHCF) occurs. Fatigue has been identified as one of the main failure modes which causes the eventual failure of the Al-alloy components [2]. Hence, increasing research efforts have been devoted in recent years to understanding the fatigue failure mechanisms and the associated microstructural evolutions in Al-alloys.

Fatigue-induced microstructural evolution underneath the fracture surfaces in the region of crack initiation and early growth is associated with the accumulated plasticity [3,4]. Plastic deformation in Al-alloys often occurs via a prevailing mechanism of dislocation glide, whereas twining normally does not take place in Al-alloys due to their high stacking fault energies [5]. An in-situ microstructural characterization during tension of nanoscale Al-Si eutectic revealed that the progression of plasticity in the alloy is accommodated by dislocation slip in the nano-Al channels [6]. A high density of tangled dislocations in the microstructure of Al alloys not only caused the hardening, but also interacted with the precipitates which affected the recrystallization behavior during hot deformation [7]. During low cycle fatigue, reversibility of dislocation slip occurred by the formation and annihilation of the Orowan loops, resulting in the cyclic softening of Al alloys [8].

In addition, it has been recognized that the deformation-induced localized solid-state amorphization is actually another important deformation mechanism [9–11]. In the extreme deformation conditions, the localized solid-state amorphization can occur at grain boundaries, along crack paths or surrounding nano-voids [11]. This is the result of lattice instability due to high elastic strain in the dislocation core regions

---

* Corresponding authors.
  E-mail addresses: qianguian@imech.ac.cn (G. Qian), zhiyangw@ansto.gov.au (Z. Wang).

[10]. The high dislocation density in a local region engenders lattice distortion which likely initiates the solid-state amorphization.

For fatigue under negative stress ratios, the cycling of tension and compression can cause a repeated process of opening, closure and contact of fatigue-induced cracks in the material. Under sufficiently large numbers of pressing cycles, a typical fractographic feature, i.e. fine granular area or rough region, was usually developed with the crack initiation and early growth [12,13]. This feature tended to decrease or even disappear as the stress ratio changes from negative to positive [14]. However, the microstructural evolution under VHCF is also closely related on the initial microstructure of the material [3]. For example, fatigue cracks are prone to initiate in equiaxed α grains of titanium alloys with a bimodal microstructure [15]. For titanium alloys with the basketweave microstructure, the fatigue fractography often shows the irregularly distributed facet-like surfaces instead of the common "fisheye" characteristics [16].

It is essential to understand the relationship between the VHCF performance and the microstructure of Al-alloys produced by particular processes. Laser Powder Bed Fusion (LPBF), has hitherto been a common additive manufacturing process for producing Al-Si alloy bulk components with a refined microstructure [17]. The microstructure of LPBF AlSi10Mg, a hypoeutectic alloy, is characterized by the dominant cellular grains of the α-Al matrix surrounded by the boundaries with Si-rich precipitates [18]. These LPBF materials contain the refined eutectic Si precipitation, distinctive from the micron-scale coarse eutectic Si particles in the counterparts produced by conventional casting approach. In-situ compression tests under a Transmission Electron Microscope (TEM) showed that the Si-rich cellular boundaries in LPBF AlSi10Mg alloy resist the dislocation movement, contributing to the strengthening of the material. Additionally, the interaction of a high-density of dislocations with the Si particles causes an abnormally high creep stress exponent [19].

Recently, Tridello et al. [20] investigated the effect of the specimen size on the VHCF response of LPBF-AlSi10Mg alloys. Their results showed that the specimen size has a significant influence on the VHCF response regardless of the building orientation. Zhang et al. [21] discussed the influence of building directions (0°, 45° and 90°) on high cycle fatigue property of LPBF-AlSi10Mg alloys, and the fatigue strength was found to decrease with the increase of building angle. Li et al. [22] analyzed the defect-induced cracking behavior in VHCF of LPBF-AlSi10Mg alloy, and the correlation between grain refinement and crack propagation path was revealed. Although the fatigue properties of LPBF-AlSi10Mg alloy materials have been studied, the evolution of the unique microstructure formed during AM in VHCF remains unclear. Further investigations are essential to address the questions such as: (1) how does the stress ratio affect the VHCF behavior? (2) what is the evolutionary behavior of the unique cellular structure during VHCF, and what is the underlying mechanism? (3) which factors in VHCF affect the evolution of the microstructure?

Therefore, understanding the microstructural evolution in the LPBF AlSi10Mg material in response to the fatigue deformation is needed to uncover the fatigue failure mechanism. In the present work, the VHCF performance and the microstructural evolutions of the LPBF AlSi10Mg alloy before and after VHCF under R = −1 and 0.5 were evaluated, with a particular focus on the VHCF-induced changes in the Si precipitation in the material.

2. Materials and methodology

Cylindrical bar specimens of AlSi10Mg materials with the dimensions of Φ16 mm × 52 mm were deposited by LPBF using a commercial EOS M280 system. The chemical compositions (wt. %) of the raw AlSi10Mg powers used in the deposition were measured to be 9.75 Si, 0.22 Mg, 0.092 Fe, 0.011 Ti, and balanced Al using Energy Dispersive X-ray Spectroscopy. The deposition processing parameters were as follows: laser power (P) of 370 W, hatch spacing (H) of 0.19 mm, scanning speed (ν) of 1300 mm/s, and layer thickness (h) of 50 μm. Further details regarding the LPBF progressing and the mechanical properties of the produced AlSi10Mg materials can be found in [23].

The initial macroscopic defects of as-built material were observed by synchrotron radiation X-ray micro-computed tomography (micro-CT) at the Shanghai Synchrotron Radiation Facility. The collected tomographic data were processed using the Avizo program to obtain the initial porosity and defect size [24]. In addition, the initial microstructure of the as-built AlSi10Mg alloy was characterized by X-ray diffraction (XRD), Scanning Electron Microscopy (SEM), electron backscatter diffraction (EBSD) and TEM. As-built metallographic specimens were mechanically polished and etched using Keller's solution for SEM examination. SEM observations using secondary electron imaging, backscattered electron imaging and EBSD were carried out in a Zeiss GeminiSEM 300. A step size of 0.5 μm was used in the EBSD scans of the as-built AlSi10Mg alloy. TEM observation was conducted using a thin foil specimen prepared from 3 mm diameter disks. These disk specimens were extracted with their normal directions perpendicular to the building direction, and then thinned down to allow electron-transparency by mechanical and twin-jet polishing.

Ultrasonic fatigue testing method was used in this study. Hourglass-shaped specimens with a minimum cross-sectional diameter of 3.5 mm were machined out for fatigue tests from the as-built cylindrical bars. A few fatigue tests were performed at room temperature on the Lasur GF20-TC ultrasonic fatigue testing machine. The fatigue tests were performed with two different stress ratios (R) of −1 and 0.5. The ultrasonic fatigue loading was controlled by displacement, and the resonant frequency of the specimen was equal to the input incitation frequency (20 k ± 500 Hz) of the ultrasonic piezoelectric ceramic resonator. However, during fatigue testing, the accumulated damage of the specimen will reduce its intrinsic resonant frequency due to the crack initiation and propagation. When the resonant frequency is lower than 19.5 kHz, the damaged specimen no longer meets the resonant frequency condition, and the ultrasonic vibration stops, that is, the fatigue test ends with the failure of the specimen.

After VHCF tests, fracture surfaces were inspected by SEM, TEM and Transmission Kikuchi Diffraction (TKD). TEM observations were performed using a high-resolution Talos F200X TEM equipped with the Energy Dispersive X-ray Spectroscopy (EDS), with the thin-foil specimens extracted near crack initiation area by focused ion beam (FIB) milling. To obtain a fine surface on the FIB cross-sectional plane, the surface of the fracture surface was first covered with a thin Pt layer for protection. The initial milling was done with a 0.79 nA Ga$^+$ ion beam current at 30 keV, which was reduced progressively to 0.23 nA for milling to a thickness of ~200 nm. The thinning was done at ~30 keV with a beam current of 80 pA to a thickness of less than 100 nm. The final polishing to reduce FIB ion beam damage was performed at 5 keV, 15 pA followed by 2 keV, 23 pA to a thickness of less than 50 nm.

Further crystallographic orientation mapping on the FIB specimen was performed using TKD in a Zeiss Auriga SEM equipped with an Oxford TKD detector using a scanning step size of 18 nm. Note that additional TEM observation was performed with the specimen extracted from as-built material by FIB milling to allow the identification of any potential change in the microstructure due to the FIBing process.

3. Results

3.1. As-built microstructure

Fig. 1 shows the photograph of the as-built materials and the results of the microstructural characterization. A section from the middle region of the as-built bar materials (Fig. 1a) was measured by synchrotron micro-CT and the reconstructed 3D image is shown in Fig. 1b. The porosity defects, marked with non-grey colors in Fig. 1b, originate from the lack of fusion defects and pores during LPBF. The overall porosity of the material was evaluated to be 0.33%. The equivalent size of the
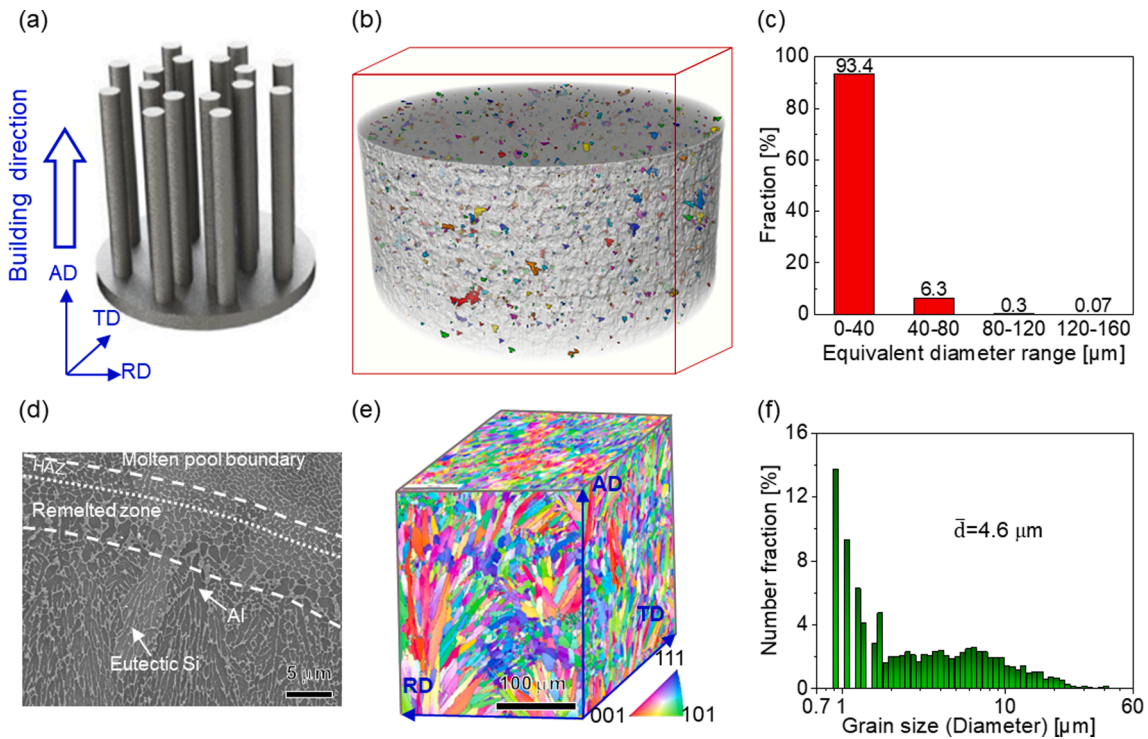
Fig. 1. (a) Photography of the as-built AlSi10Mg materials, (b) 3D synchrotron micro-CT image showing the porosity defects in the as-built material, (c) number fractions of porosity defects as a function of their equivalent diameters, (d) back-scattered image showing microstructure around the molten pool boundary, (e) EBSD IPF orientation map and (f) statistical distribution of grain sizes of the as-built material. AD, RD and TD denote the axial, tangential and radial directions, respectively.

defects is evaluated as the diameter of a sphere with the same volume [25], and its statistical distribution is presented in Fig. 1c. The micro-CT analysis shows that the average equivalent diameter of most porosity defects is less than ~40 μm.

Fig. 1d shows the SEM micrograph of the as-built material. Due to the layer-by-layer deposition process and the resultant different local thermal histories experienced at the inner and boundary of molten pools [26], a hierarchical microstructure around the molten pool boundary is observed, consisting of dendritic-like eutectic microstructure in the molten pool and cellular eutectic microstructure around its boundary. The cellular microstructure shows various sizes, with a coarse structural band (referred to the remelted zone) and a region that partially decomposed into globular Si particles (referred to the heat affected zone, HAZ). EBSD analysis (Fig. 1e) reveals that the dominant columnar grains tend to grow along the building direction, and the minor equiaxed grains are presented near the molten pool boundaries. This is because of the cyclic thermal loading and the remelting processes experienced during the deposition of subsequent layers, leading to the recrystallized

equiaxed grain formation near the layer-to-layer molten pool boundaries [27]. Fig. 1f shows the statistical distribution of the Al matrix grain sizes obtained from EBSD observations, showing an average grain size of ~4.6 μm.

Fig. 2(a-c) further shows the TEM observation of cellular structures in the as-built material. The dark-field TEM image (Fig. 2b) indicates that the as-built material is characterized by a cellular microstructure with the precipitates randomly distributed along the cellular network boundaries. The elemental mapping of Si (Fig. 2c) confirms that the as-built cellular microstructure consists of the Si-rich precipitates at the boundaries, consistent with the near-eutectic microstructural nature of studied AlSi10Mg alloy. XRD results indicate that the as-built material consists of Al and Si phases (see the Supplementary Fig. S1).

3.2. Microstructure of fatigued specimens

The S-N data (Fig. 3a) shows that the fatigue life of the as-built alloy increases as the applied stress amplitude decreases for both R = −1 and
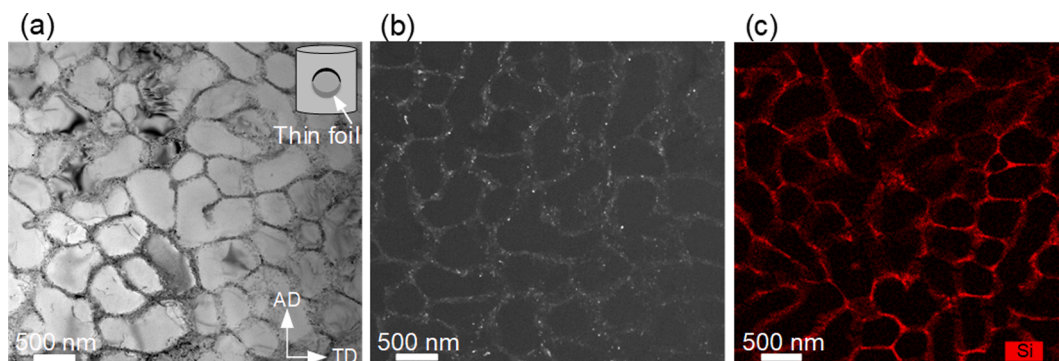

Fig. 2. (a) Bright-field and (b) dark-field TEM images and (c) Si elemental distribution map of the as-built specimen.
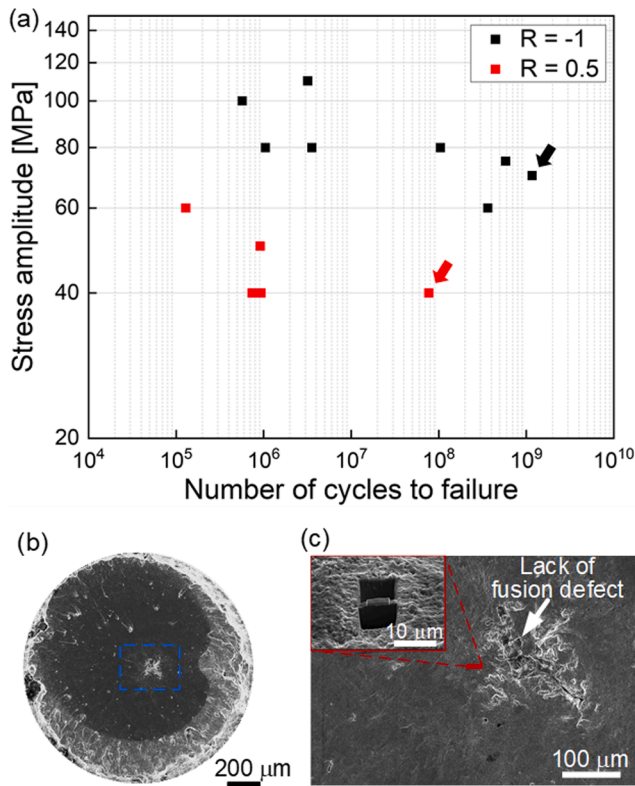
Fig. 3. (a) *S-N* data of fatigue tests with stress ratios R = −1 and 0.5, (b) fracture morphologies of a representative specimen after 1.17×10^9 fatigue cycles at $S = 70$ MPa. (c) A closed-view of the crack initiation area in (b).

0.5. Based on the fatigue tests in the present condition, under R = −1, the VHCF of the as-built material which shows the fatigue life beyond 10^7 cycles normally occurs under an applied stress amplitude below 80 MPa. At higher stress levels (80–110 MPa), the high-cycle fatigue with the fatigue life less than 10^7 cycles occurs. As the stress ratio increases, the fatigue resistance decreases significantly from 80 MPa to 40 MPa at a fatigue life-time of $N_f = 10^8$ cycles.

The fatigue fractographic observations demonstrate that the fatigue cracking of the investigated specimens initiated at the lack of fusion defects. We presented the representative microstructural results from the specimens after 1.17×10^9 fatigue cycles under R = −1 and the 7.7×10^7 cycles under R = 0.5 in the following, corresponding to the fatigue condition indicated by the black and red arrows in Fig. 3a. Additional fractographic observations of other fatigue test conditions can be found in the Supplementary Fig. S2-4. As represented by the fractographic observations in Fig. 3b, the cracks were mainly initiated inside the specimen under the present VHCF conditions. The characteristic "fish-eye" morphology indicative of the crack initiation and propagation processes was observed on the fracture surface (Fig. 3b). Note that a close inspection of the "fish-eye" region confirms that the presence of the lack of fusion defect in the LPBF specimens promoted the initiation of VHCF cracking (Fig. 3c), which is consistent with previous studies on fatigue of LPBF alloys [28]. This finding implies the significance of eliminating manufacturing defects in the materials for improving their fatigue performance.

The microstructure of fatigued specimens was further characterized by TEM. We focused on two fatigue test conditions of the 1.17×10^9 fatigue cycling under R = −1 and the 7.7×10^7 cycles under R = 0.5, as marked in the *S-N* data (Fig. 3a) with black and red arrows, respectively. Fig. 3c presents a typical example of the fatigue fracture surface morphology under R = −1. The lifting-out position of thin-foil FIB specimens for further TEM and TKD observations is close to crack source, as shown in Fig. 3c.

3.2.1. Microstructural evolution under R = 0.5

For VHCF specimen with R = 0.5, the bright-field TEM image (Fig. 4a) reveals similar microstructures to the as-built material (Fig. 2a), i.e. the fatigued microstructure in this condition remains to exhibit the cellular structures with the precipitates distributed along the cellular network boundaries. Further, a closed-view of the box area in Fig. 4a was performed. The obtained result in Fig. 4b shows that the size of the precipitates on the cellular network boundaries appears to be similar to that in the as-built material. The corresponding TKD-based orientation map of the same region as in Fig. 4a is shown in Fig. 4c. The results indicate that there is no significant misorientation development. No obvious plastic deformation occurred near the fracture surface, and the misorientation within the grains is relatively uniform. The density of geometrically necessary dislocations (GNDs) was estimated based on the lattice curvature following the approach described in Ref. [29]. Fig. 4d presents the determined GNDs density distribution corresponding to Fig. 4c. No appreciable accumulation of GNDs was observed within the Al grains in this condition.

3.2.2. Microstructural evolution under R = −1

For the VHCF specimen under R = −1, a first look at the TEM microstructural results (Fig. 5a) reveals similar microstructures to the as-built condition (Fig. 2b), i.e. the fatigued specimen is still characterized by the cellular structures with the precipitates randomly distributed along the cellular network boundaries. Fig. 5b further presents the Si elemental distribution in the same observation region of Fig. 5a. High-resolution (HR)-TEM analyses were performed around the "G" location marked in Fig. 5a and b. The two observed positions are HR1 within the cell structure and HR2 on the cellular network boundary, as indicated in Fig. 6a. The observation positions of HR1 and HR2 regions are approximately 0.5 and 0.7 μm away from the fracture surface, respectively. HRTEM image of HR1 is displayed in Fig. 6b. A number of stacking faults (SFs) were observed in the HRTEM image of Al matrix (Fig. 6), as marked by arrows. Fig. 6c further shows the Inverse Fast Fourier Transformation (IFFT) image and Fast Fourier Transformation (FFT) image corresponding to the dashed area in Fig. 6b. It indicates that these are SFs parallel to one of the (1 1 1) planes corroborated by streaking parallel to ⟨1 1 1⟩ in the FFT of the corresponding image (the inset of Fig. 6c). The Al phase on the cellular network boundary was also noticed to contain a number of SFs as shown in the HRTEM image in Fig. 6d. The formation of SFs has also been observed in the Al-Mg-Si alloy subjected to the equal-channel angular pressing [30]. These SFs are possibly formed among partial dislocations in the Al alloys due to the severe plastic deformation.

Fig. 7a shows the TKD-based orientation map of the fatigued specimen near the fracture surface. A layer of fine Al grains with sizes varying from tens to hundreds nm underneath the fracture surface was observed, indicating that the refinement of matrix grains occurs during VHCF. In addition, the low-angle grain boundaries identified with misorientation between 2° and 15° were observed, which are presumably due to the accumulation of dislocations during VHCF. The corresponding GNDs density distribution of Fig. 7a is shown in Fig. 7b. Fig. 7c presents the dislocation configurations by TEM near the fracture surface (as marked by the letter H in Fig. 7a), and the sub-grain boundaries were observed. Compared with Fig. 7b and c, it is found that the dislocation density in the grains near the crack surface is locally concentrated to form sub-grain boundaries, as shown by the red line in the Fig. 7b. This implies that the local dislocation accumulation in the grains near the crack surfaces promotes the evolution of sub-grain boundaries to low-angle boundaries and high-angle boundaries.

Fig. 8 shows a further close inspection of the Si-precipitation behavior after VHCF. The morphologies of Si particles at a distance of ~2.8 μm from the fracture surface (Fig. 5a) are similar to those of the as-built material (Fig. 2b), i.e. the cellular boundaries compose of close-packed Si precipitates. Fig. 8b shows the TEM observation at a higher magnification corresponding to the dashed box area in Fig. 8a, as well as
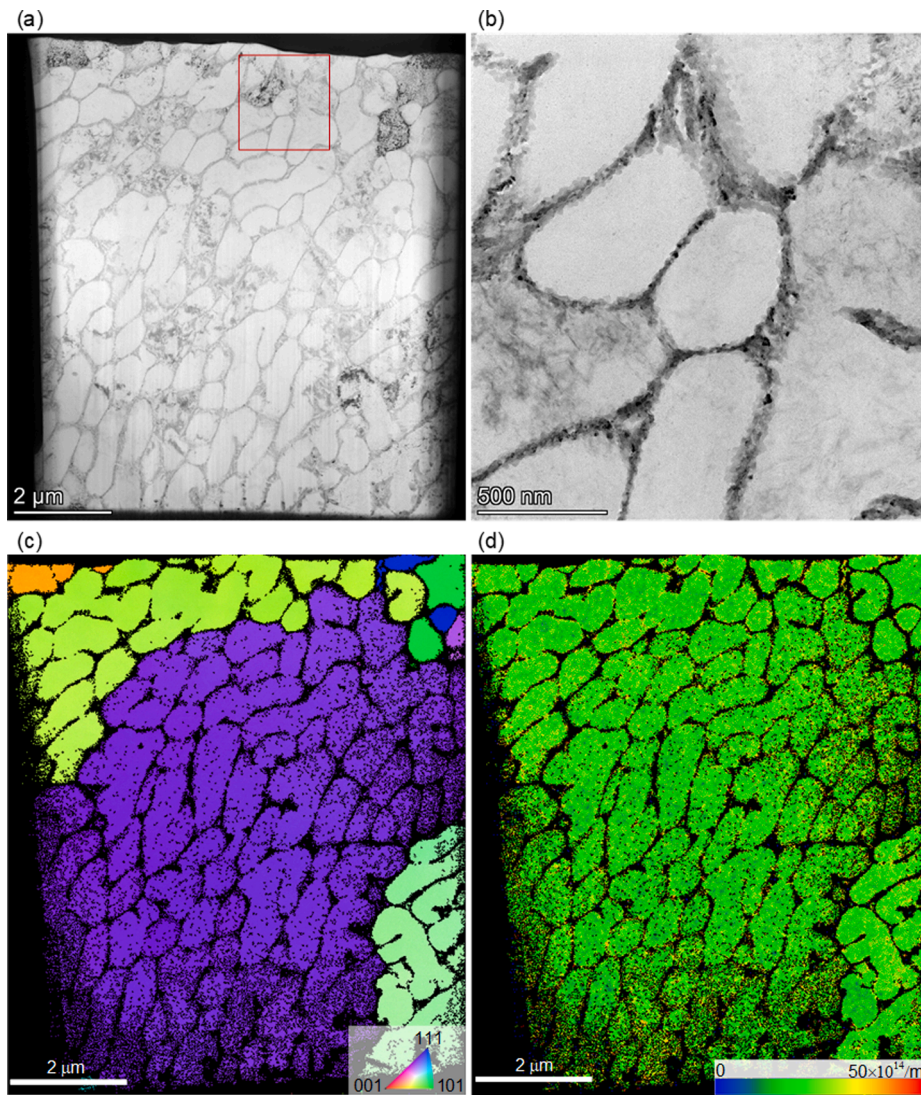
Fig. 4. (a) Bright-field TEM image for fatigued specimen with R = 0.5, (b) a closed-view of the box area in (a), (c) TKD-based orientation map corresponding to (a), (d) GND distribution in the same region of (c).
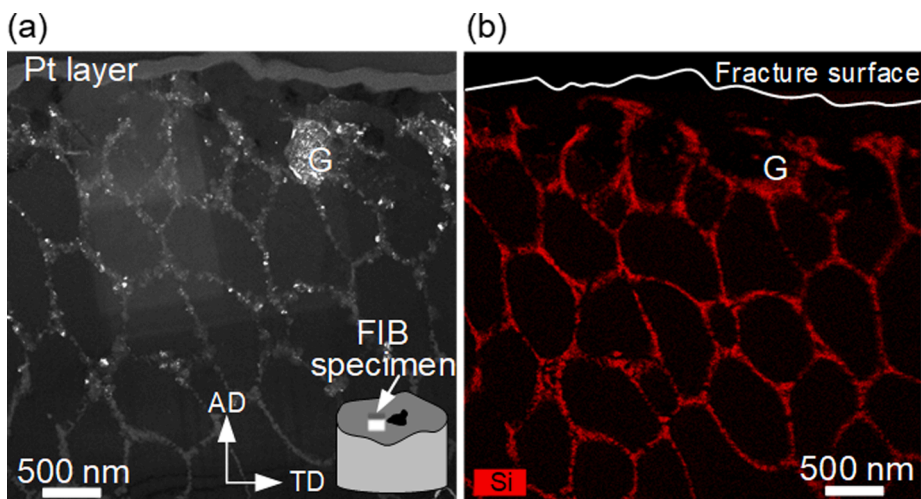

Fig. 5. (a) Dark-field TEM image and (b) Si elemental distribution map of the VHCF specimen with R = −1.
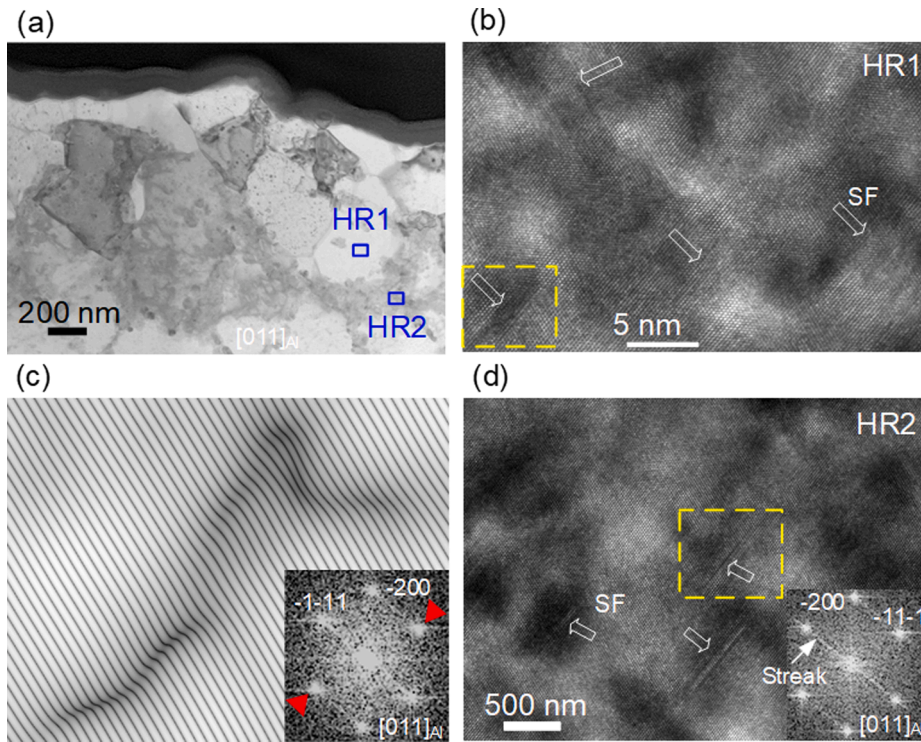
Fig. 6. (a) TEM image showing two HRTEM observation positions of HR1 within the cell structure and HR2 on the cellular network boundary, (d) HRTEM image for HR1, (e) Inverse Fast Fourier Transformation image together with the Fast Fourier Transformation image (inset) corresponding to the dash box area in d, (f) HRTEM image for HR2 with the Fast Fourier Transformation image corresponding to the dashed area.

the selected area electron diffraction (SAED) pattern of the Si particles. The SAED data shows diffuse halo rings, suggesting the amorphous nature of the precipitates. The amorphous Si-precipitates was frequently observed (see the Supplementary Fig. S5). Fig. 8c and e further present the HRTEM images of the Areas 1 and 2 in Fig. 8b, respectively. The white dashed lines marked the boundaries of crystalline Si and amorphous regions. A HRTEM analysis was further conducted to reveal the distribution of defects induced by fatigue deformation. Lattice defects generally produce the lattice strain, which can be evaluated through the geometric phase analysis (GPA) of HRTEM images [31]. Fig. 8d and f show the GPA strain maps of the white-box regions in Fig. 8c and e, respectively. The color scale in the bottom of the Fig. 8d and f shows the magnitude of the lattice strain, in which the positive values indicate the tensile strain whereas the negative values mean the compression strain. As confirmed by Fig. 8d and f, a significant strain gradient and large local strain field occurs at the fatigue fracture surface under R = −1.

4. Discussion

4.1. Development of fine-grained layer

It is believed that the grain refinement in VHCF is associated with the high-angle-boundary formation process. The models interpreting the formation mechanism of the fine-grained layer at the fracture surface of VHCF have been proposed [4,32–34], among which the numerous cyclic pressing (NCP) model [4] is generally accepted for providing a rationale for the formation of the fine-grained layer and its dependence on the applied stress ratio or compression stress. According to the NCP model, repeated contact stress between the crack surfaces and a sufficient number of tension-compression loading cycles experienced during VHCF are responsible for the grain refinement. The resultant local severe plastic deformation will result in the accumulation of a large number of dislocations, promoting the development of high-angle boundaries and the formation of fine-grained layer, as observed in Fig. 7. However, for R

= 0.5, there is no pressing of crack surfaces due to its positive stress ratio, resulting in insufficient local plastic accumulation to form large angle grain boundaries. According to the TKD analysis results of R = −1 and 0.5, the GND density is statistically analyzed and shown in Fig. 9. The mean GND densities of fatigued specimen with R = −1 is estimated to be $\rho_{mean} = \sim 29.40 \times 10^{14}\,\mathrm{m}^{-2}$, while that for the specimen of R = 0.5 is a bit lower ($\rho_{mean} = \sim 20.82 \times 10^{14}\,\mathrm{m}^{-2}$). In particular, the local accumulation of dislocations at fracture is more significant (Fig. 7b) due to the repeated cycling process of crack opening, closure and contact under R = −1. The results indicate that the strain gradient is more severe in the fatigued specimen with R = −1 than that of R = 0.5, leading to a higher density of GNDs as well as the formation of fine-grained layer.

4.2. Fatigue-induced Si particle growth

Interestingly, the size of the Si precipitate on the cell boundaries near the fracture surface of fatigued specimen with R = −1 (Fig. 5a) is shown to be larger than that of R = 0.5 (Fig. 4b). Based on the analysis of the TEM dark field images, we further estimated the diameter of the Si precipitates and the results are shown in Fig. 10. Despite the limitations of TEM for statistical analysis, the coarsening of Si precipitates is identifiable after VHCF with R = −1.

Previous results show that the temperature rise is less than 50 °C measured by infrared thermography for aluminum alloys under 20 kHz fatigue loading [35,36]. Therefore, the thermal effects on the Si precipitate growth observed in aluminum alloys during fatigue tests can be ignored. It is inferred that the growth of Si particles in the alloy observed under R = −1 is likely occurred as a consequence of the severe plastic deformation near the fracture surface under this negative stress ratio. Therefore, a high density of dislocations present in the vicinity of the fracture surface can promote the solute pipe diffusion and the nucleation of precipitates at the dislocation cores. The dislocation motion will lead to the generation of vacancies due to dragging of dislocation jogs, and the injection of vacancies will mediate the solute diffusion and
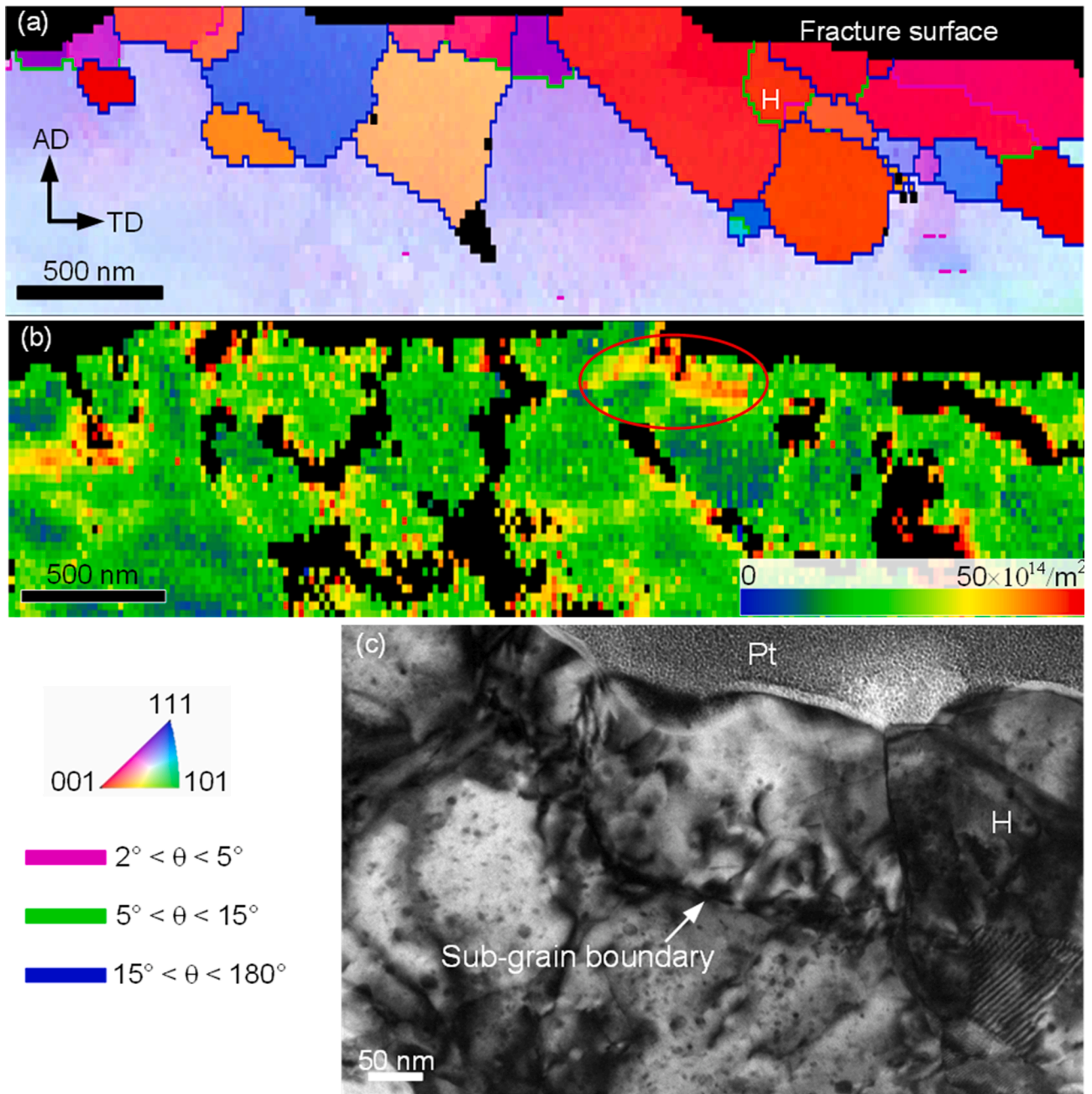
Fig. 7. (a) TKD-based orientation map showing the microstructure near fracture surface of VHCF specimen with R = −1, (b) GND distribution corresponding to (a), (c) dislocation configurations near the H area in (a).

precipitation [37,38]. In this study, cyclic pressing of crack surfaces under R = −1 caused the accumulation of local strain underneath the crack surface. To accommodate local plastic deformation, the dislocations are generated in the microstructure [32,34]. Therefore, the solute diffusion will be accelerated by the non-equilibrium vacancies, dislocations and grain boundaries. The high-density vacancies introduced by cyclic pressing of crack surfaces under R = −1 facilitate fast redistribution of Si solutes, leading to the coarsening of Si particles on the cellular network boundaries.

4.3. Si precipitation amorphization

The amorphization has been observed in various metallic alloys experiencing plastic deformation [11,39–41] or ion irradiation [42]. To clarify whether the readily observed Si-precipitate amorphization in the

TEM observation of the FIB-extracted specimen from fatigued AlSi10Mg is caused by VHCF or an artefact due to the Ga ion irradiation during the FIB milling process used for preparing the TEM specimens, additional TEM measurements were performed for the as-built material with the specimen prepared by FIB milling (see the Supplementary Fig. S5). A comparison of the obtained TEM results with those from the FIB specimen of the fatigued material confirms that the readily observed amorphization of Si-precipitates in the fatigued AlSi10Mg alloy is truly occurred due to the VHCF process rather than an artefact due to the specimen preparation by the FIB milling. It is well-accepted that a high concentration of dislocation defects plays a crucial role in the amorphization of alloys [9,11]. When the dislocation density in metallic materials achieves some critical values (for example, 10^{18} m^{-2} for Ti alloys [43]), the crystal structure would collapse and transform into a localized amorphous structure so as to release the high elastic strain. Previous
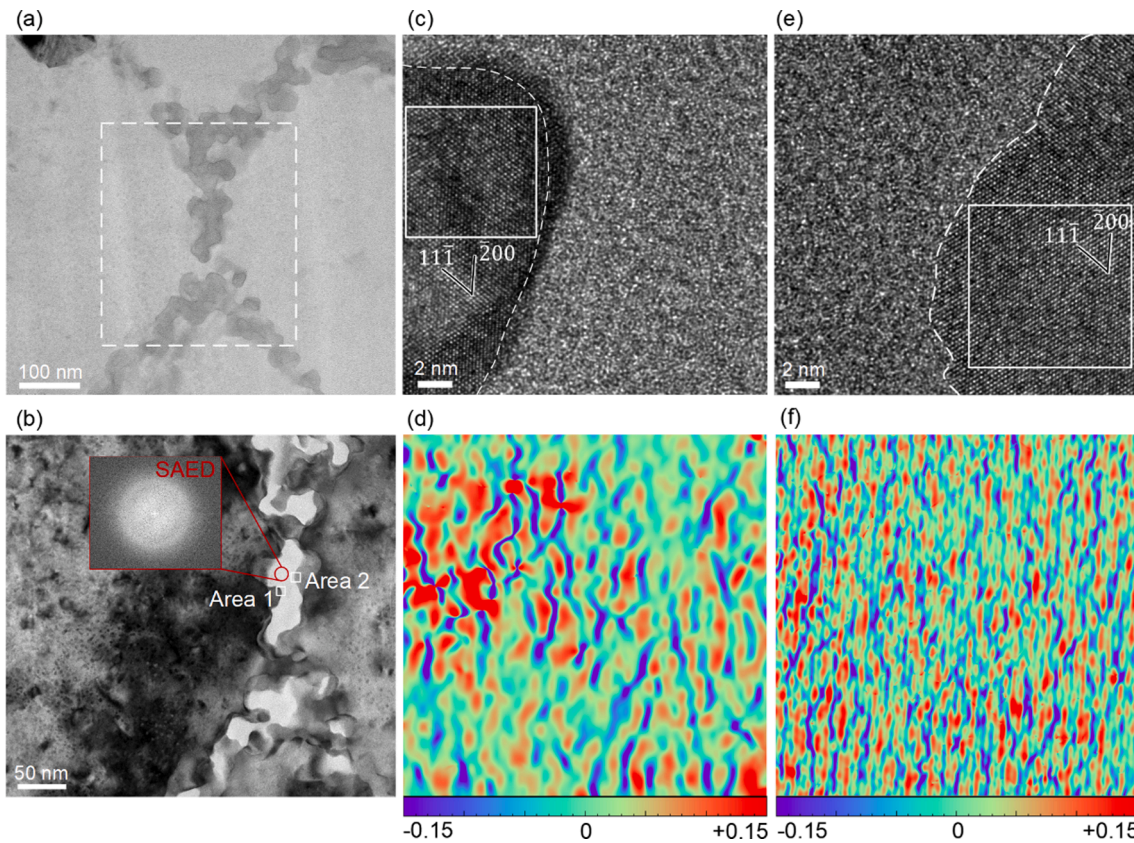
Fig. 8. (a) Si precipitates at the cellular grain boundaries at a distance of ~2.8 μm from the fracture surface for fatigued specimen with R = −1. (b) A closed-view of the dashed box area in (a). HRTEM images of Area 1 and (f) Area 2 indicated in (b). GPA strain map imaged by [200] of the white-box regions in (d) Area 1 and (f) Area 2.
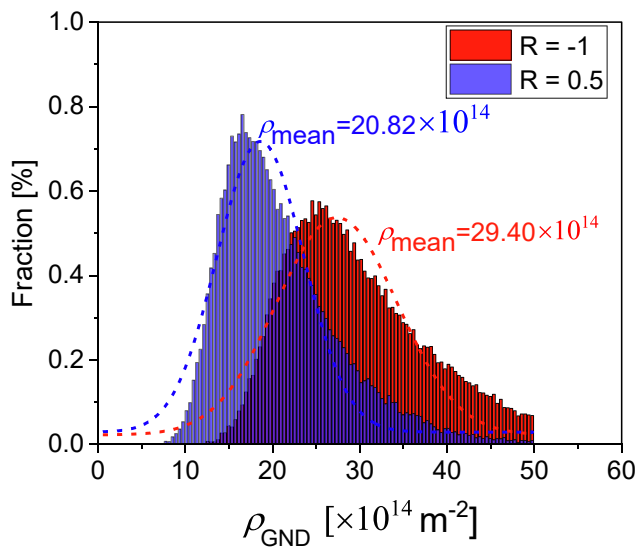

Fig. 9. Distribution of discrete GND density determined from TKD-based measurements at the fracture surface of fatigued specimens.

Fig. 10. Measurement of the equivalent diameter of Si precipitates in the as-built microstructure and at the fatigue-induced fracture surfaces under R = −1 and 0.5.

molecular dynamics simulations [37,42] also supported that the dislocation accumulation contributes significantly to the atomic disorder and lattice strain, leading to an elastic softening and final collapse of the crystalline structure [39,44]. For the Si precipitates, due to their closed-packed arrangement in the microstructure and strong encumbrance for dislocation movements stemming from copious interfaces such as grain boundaries, dislocations tend to be concentrated in a small deformation
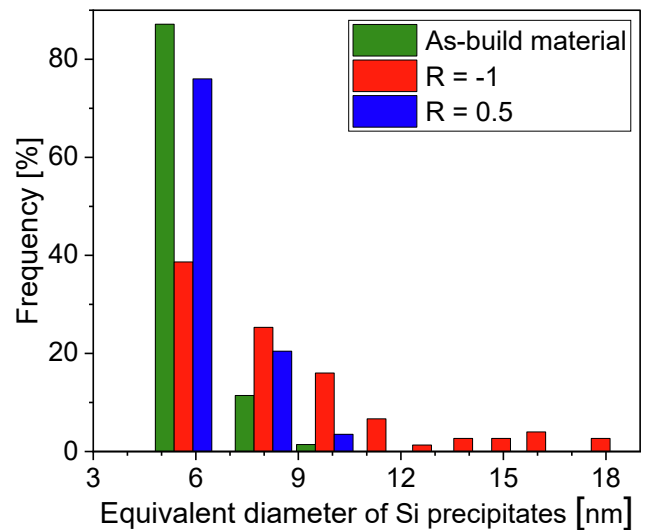
volume, leading to the heavily dislocated structure and the resultant amorphization. The amorphization of Si-precipitates in AlSi10Mg may dissipate the strain energies during VHCF, leading to the delay of the fatigue cracking developed in the alloy, and thereby increasing its fatigue resistance.

4.4. Effect of stress ratio on VHCF microstructural evolution

In the present study, it is demonstrated that VHCF with R = −1 exhibits a microstructural characteristic distinct from that of R = 0.5. In the former case, the applied negative stress ratio in the fatigue test greatly affects the microstructural evolution at the fracture surface. Fig. 11 schematically shows the microstructural evolution of VHCF with R = −1 and 0.5. In the as-build material, closed-packed Si precipitates are distributed along the cellular network boundaries, as shown in Fig. 11a and d. Once a crack is initiated, the crack surfaces will be cyclically pressured under tension-compression loading and thus induce local severe plastic deformation. Therefore, dislocation slip in Al grains and Si precipitates was activated, resulting in the development of lattice defects and misorientation in Si precipitates (Fig. 11b). With the accumulation of local strain, the dislocation in Al phase caused pile-ups at the cell boundaries. When the intensified stress that originated from pile-up dislocations in the Al phase was excessive, SFs would form, as observed in HRTEM images in Fig. 6b and d. For the Si precipitates, closed-packed arrangement along the cellular network boundaries, dislocation movement was strongly hindered due to copious interfaces such as grain boundaries. Dislocations tended to be accumulated in a small deformation volume. When the defect density in the Si precipitates reaches a critical level, they generate islands of amorphous material, Fig. 11c. Under the cyclic loading of ultra-long cycles, the high-density dislocation introduced by cyclic pressing of crack surfaces developed into sub-grain boundaries (Fig. 11c) and eventually formed large-angle grain boundaries, and grain refinement near the crack surfaces occurred.

In contrast, for R = 0.5, the specimen is in pull-pull loading mode, that is, there is no cyclic pressing on the crack surface. The plastic deformation near the crack surface is significantly smaller than in the case of R = −1. Therefore, fewer dislocations are activated (Fig. 11e and f), as determined in Fig. 9. In addition, the tensile stress under R = 0.5 promoted crack growth. This is the main reason for the decreased fatigue life and no grain refinement on fracture surfaces.

5. Conclusions

In this study, the effect of stress ratio on the VHCF performance of LPBF AlSi10Mg alloy was investigated. The microstructural evolution underneath the fracture surfaces in the region of crack initiation and early growth is characterized and discussed. The main conclusions are summarized as follows:

(1) VHCF sample with R = −1 exhibit a microstructural characteristics distinct from that of R = 0.5, and that the negative stress ratio greatly affects the VHCF performance and microstructural evolution at the fracture surface. The pull-pull loading mode without cyclic pressing of crack surfaces under R = 0.5 promoted crack growth, resulting in a decrease in fatigue life. Only few dislocations were observed near the crack surfaces under R = 0.5, which is due to the fact that there is no cyclic pressing of crack surfaces and the resultant severe plastic deformation.

(2) Under R = −1, a fine-grained layer of Al was developed in the "fish-eye" region of the fracture surface as a result of severe plastic deformation, and stack faults were observed in Al matrix under VHCF. Coarsening Si precipitates on the cellular network boundaries presented near the fracture surface due to the dynamic precipitation. This is rationalized by the generation of lattice defects including dislocation and sub-grain boundary during VHCF which mediate the solute diffusion and precipitation.
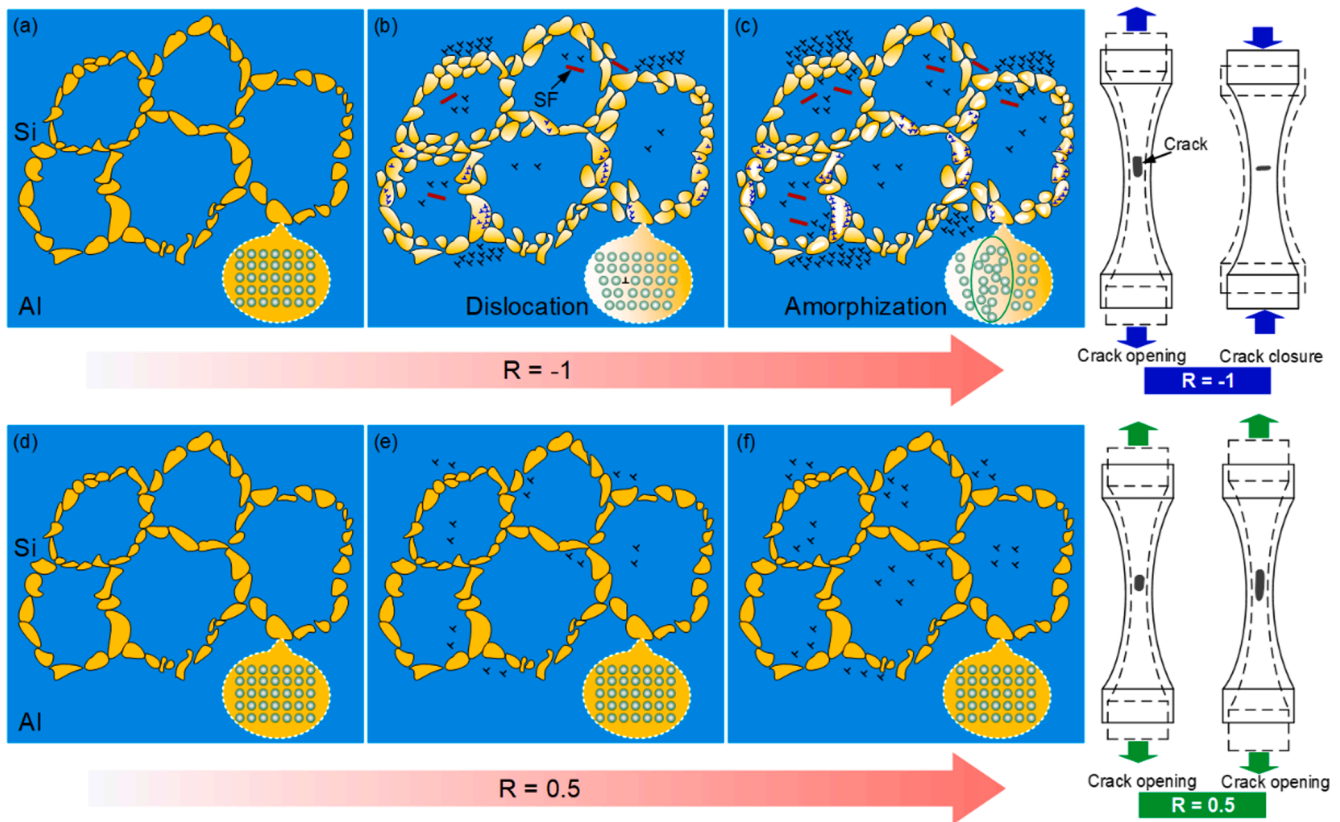

Fig. 11. A schematic showing the microstructural evolution during VHCF under R = −1 and 0.5: (a) and (e) initial Si precipitates on the cellular network boundaries, (b) activation of dislocations and formation of stacking fault for Al phase, and plastic deformation and growth of Si particles, (c) amorphization of Si precipitates and formation of sub-grain boundaries under R = −1. (e) Activation of dislocations and (f) dislocations pile-up for Al phase under R = 0.5.

(3) Amorphization of Si precipitates occurred under R = −1, which is notably different from the microstructure evolution of low cycle fatigue. Due to the limited spaces offered by nano-sized Si particles and strong encumbrance for dislocation movements, dislocations from multiple sources always concentrate to a small deformation volume, leading to extremely high local dislocation density and local amorphization.

Declaration of Competing Interest

The authors declare that they have no known competing financial interests or personal relationships that could have appeared to influence the work reported in this paper.

Data availability

Data will be made available on request.

Acknowledgements

Appendix A. Supplementary data

Supplementary data to this article can be found online at https://doi.org/10.1016/j.ijfatigue.2022.107167.

References

[1] Barrirero J, Pauly C, Engstler M, Ghanbaja J, Ghafoor N, Li J, et al. Eutectic modification by ternary compound cluster formation in Al-Si alloys. Sci Rep 2019;9 (1). https://doi.org/10.1038/s41598-019-41919-2.

[2] Suresh S. Fatigue of materials. 2nd ed. UK: Cambridge University Press; 1998.

[3] Pan XN, Xu SW, Qian GA, Nikitin A, Shanyavskiy A, Palin-Luc T, et al. The mechanism of internal fatigue-crack initiation and early growth in a titanium alloy with lamellar and equiaxed microstructure. Mater Sci Eng A 2020;798:140110. https://doi.org/10.1016/j.msea.2020.140110.

[4] Hong YS, Liu XL, Lei ZQ, Sun CQ. The formation mechanism of characteristic region at crack initiation for very-high-cycle fatigue of high-strength steels. Int J Fatigue 2016;89:108–18.

[5] Zhang ZJ, Zhang P, Li LL, Zhang ZF. Fatigue cracking at twin boundaries: Effects of crystallographic orientation and stacking fault energy. Acta Mater 2012;60(6-7): 3113–27.

[6] Wei BQ, Wu WQ, Xie DY, Lien H, Kayitmazbatir M, Misra A, et al. In situ characterization of tensile behavior of laser rapid solidified Al–Si heterogeneous microstructures. Mater Res Lett 2021;9(12):507–15.

[7] Shaha SK, Czerwinski F, Kasprzak W, Friedman J, Chen DL, Shalchi-Amirkhiz B. Interaction between nano-precipitates and dislocations during high temperature deformation of Al-Si alloys. J Alloys Compd 2017;712:219–24.

[8] Nandy S, Sekhar AP, Kar T, Ray KK, Das D. Influence of ageing on the low cycle fatigue behaviour of an Al–Mg–Si alloy. Philos Mag 2017;97(23):1978–2003.

[9] Zhao ST, Li ZZ, Zhu CY, Yang W, Zhang ZR, Armstrong DEJ, et al. Amorphization in extreme deformation of the CrMnFeCoNi high-entropy alloy. Sci Adv 2021;7(5). https://doi.org/10.1126/sciadv.abb3108.

[10] Wu XL, Tao N, Hong YS, Lu J, Lu K. Localized solid-state amorphization at grain boundaries in a nanocrystalline Al solid solution subjected to surface mechanical attrition. J Phys D: Appl Phys 2005;38(22):4140–3.

[11] Han S, Zhao L, Jiang Q, Lian JS. Deformation-induced localized solid-state amorphization in nanocrystalline nickel. Sci Rep 2012;2:493–8.

[12] Pan XN, Su H, Sun CQ, Hong YS. The behavior of crack initiation and early growth in high-cycle and very-high-cycle fatigue regimes for a titanium alloy. Int J Fatigue 2018;115:67–78.

[13] Cong T, Qian GA, Zhang G, Wu S, Pan XN, Du LM, et al. Effects of inclusion size and stress ratio on the very-high-cycle fatigue behavior of pearlitic steel. Int J Fatigue 2021;142:105958. https://doi.org/10.1016/j.ijfatigue.2020.105958.

[14] Ritz F, Stäcker C, Beck T, Sander M. FGA formation mechanism for X10CrNiMoV12-2-2 and 34CrNiMo6 for constant and variable amplitude tests under the influence of applied mean loads. Fatigue Fract Eng Mater Struct 2018;41 (7):1576–87.

[15] Nalla RK, Ritchie RO, Boyce BL, Campbell JP, Peters JO. Influence of microstructure on high-cycle fatigue of Ti-6Al-4V: Bimodal vs. lamellar structures. Metall Mater Trans A 2002;33(3):899–918.

[16] Zuo JH, Wang ZG, Han EH. Effect of microstructure on ultra-high cycle fatigue behavior of Ti–6Al–4V. Mater Sci Eng A 2008;473(1-2):147–52.

[17] Hadadzadeh A, Amirkhiz BS, Langelier B, Li J, Mohammadi M. Microstructural consistency in the additive manufactured metallic materials: A study on the laser powder bed fusion of AlSi10Mg. Addit Manuf 2021;46:102166. https://doi.org/10.1016/j.addma.2021.102166.

[18] Wu J, Wang XQ, Wang W, Attallah MM, Loretto MH. Microstructure and strength of selectively laser melted AlSi10Mg. Acta Mater 2016;117:311–20.

[19] Wu H, Ren YJ, Ren JY, Liang LX, Li RD, Fang QH, et al. Selective laser melted AlSi10Mg alloy under melting mode transition: Microstructure evolution, nanomechanical behaviors and tensile properties. J Alloys Compd 2021;873: 159823. https://doi.org/10.1016/j.jallcom.2021.159823.

[20] Tridello A, Fiocchi J, Biffi CA, Rossetto M, Tuissi A, Paolino DS. Size-effects affecting the fatigue response up to 10^9 cycles (VHCF) of SLM AlSi10Mg specimens produced in horizontal and vertical directions. Int J Fatigue 2022;160:106825. https://doi.org/10.1016/j.ijfatigue.2022.106825.

[21] Zhang YC, Li XL, Yuan SH, Sun R, Sakai T, Lashari MI, et al. High-cycle-fatigue properties of selective-laser-melted AlSi10Mg with multiple building directions. Int J Mech Sci 2022;224:107336. https://doi.org/10.1016/j.ijmecsci.2022.107336.

[22] Li JH, Sun JY, Qian GA, Shi LT. Defect-induced cracking and fine granular characteristics in very-high-cycle fatigue of laser powder bed fusion AlSi10Mg alloy. Int J Fatigue 2022;158:106770. https://doi.org/10.1016/j.ijfatigue.2022.106770.

[23] Qian GA, Jian ZM, Qian YJ, Pan XN, Ma XF, Hong YS. Very-high-cycle fatigue behavior of AlSi10Mg manufactured by selective laser melting: Effect of build orientation and mean stress. Int J Fatigue 2020;138:105696. https://doi.org/10.1016/j.ijfatigue.2020.105696.

[24] Bao J, Wu S, Withers PJ, Wu Z, Li F, Fu Y, et al. Defect evolution during high temperature tension-tension fatigue of SLM AlSi10Mg alloy by synchrotron tomography. Mater Sci Eng A 2020;792:139809. https://doi.org/10.1016/j.msea.2020.139809.

[25] Kumar P, Ramamurty U. High cycle fatigue in selective laser melted Ti-6Al-4V. Acta Mater 2020;194:305–20.

[26] Delahaye J, Tchuindjang JT, Lecomte-Beckers J, Rigo O, Habraken AM, Mertens A. Influence of Si precipitates on fracture mechanisms of AlSi10Mg parts processed by Selective Laser Melting. Acta Mater 2019;175:160–70.

[27] Wen SF, Li S, Wei QS, Yan CZ, Zhang S, Shi YS. Effect of molten pool boundaries on the mechanical properties of selective laser melting parts. J Mater Process Technol 2014;214(11):2660–7.

[28] Nadot Y, Nadot-Martin C, Kan WH, Boufadene S, Foley M, Cairney J, et al. Predicting the fatigue life of an AlSi10Mg alloy manufactured via laser powder bed fusion by using data from computed tomography. Addit Manuf 2020;32:100899. https://doi.org/10.1016/j.addma.2019.100899.

[29] Kubin LP, Mortensen A. Geometrically necessary dislocations and strain-gradient plasticity: a few critical issues. Scr Mater 2003;48(2):119–25.

[30] Liu MP, Roven HJ, Yu YD, Werenskiold JC. Deformation structures in 6082 aluminium alloy after severe plastic deformation by equal-channel angular pressing. Mater Sci Eng A 2008;483-484:59–63.

[31] Hirth JP, Lothe J. Theory of Dislocations. 2nd ed. New York: Wiley; 1983.

[32] Zhang HJ, Yu F, Li SX, He EG. Fine granular area formation by damage-induced shear strain localization in very-high-cycle fatigue. Fatigue Fract Eng Mater Struct 2021;44(9):2489–502.

[33] Sun CQ, Song QY, Zhou LL, Liu JL, Wang Y, Wu XL, et al. The formation of discontinuous gradient regimes during crack initiation in high strength steels under very high cycle fatigue. Int J Fatigue 2019;124:483–92.

[34] Li W, Sun R, Wang P, Li XL, Zhang YC, Hu TY, et al. Subsurface faceted cracking behavior of selective laser melting Ni-based superalloy under very high cycle fatigue. Scr Mater 2021;194:113613. https://doi.org/10.1016/j.scriptamat.2020.11.001.

[35] Krewerth D, Weidner A, Biermann H. Application of in situ thermography for evaluating the high-cycle and very-high-cycle fatigue behaviour of cast aluminium alloy AlSi7Mg (T6). Ultrasonics 2013;53(8):1441–9.

[36] Wagner D, Ranc N, Bathias C, Paris PC. Fatigue crack initiation detection by an infrared thermography method. Fatigue Fract Eng Mater Struct 2010;33:12–21.

[37] Liu MW, Zheng RX, Xiao WL, Li J, Li GD, Peng QM, et al. Bulk nanostructured Al-Si alloy with remarkable improvement in strength and ductility. Scr Mater 2021;201: 113970. https://doi.org/10.1016/j.scriptamat.2021.113970.

[38] Jin SB, Luo ZJ, An XH, Liao X, Li JH, Sha G. Composition-dependent dynamic precipitation and grain refinement in Al-Si system under high-pressure torsion. J Mater Sci Technol 2021;68:199–208.

[39] Wang H, Chen DK, An XH, Zhang Y, Sun SJ, Tian YZ, et al. Deformation-induced crystalline-to-amorphous phase transformation in a CrMnFeCoNi high-entropy alloy. Sci Adv 2021;7(14). https://doi.org/10.1126/sciadv.abe3105.

[40] Komatsu M, Kiritani M. Amorphization of eutectic alloys by shock compression. Mater Sci Eng A 2003;350(1-2):150–4.

[41] Wang YC, Zhang W, Wang LY, Zhuang Z, Ma E, Li J, et al. In situ TEM study of deformation-induced crystalline-to-amorphous transition in silicon. NPG Asia Mater 2016;8(7):e291–7.

[42] Huang J, Loeffler M, Muehle U, Moeller W, Mulders JJL, Kwakman LFT, et al. Si amorphization by focused ion beam milling: Point defect model with dynamic BCA simulation and experimental validation. Ultramicroscopy 2018;184:52–6.

[43] Wei C, Sun QY, Xiao L, Sun J. Deformation-induced grain refinement and amorphization in Ti-10V-2Fe-3Al alloy. Metall Mater Trans A 2012;43(1):316–26.

[44] Li M. Defect-induced topological order-to-disorder transitions in two-dimensional binary substitutional solid solutions: A molecular dynamics study. Phys Rev B 2000;62:13979–95.